UC Berkeley
UC Berkeley Previously Published Works

Title

A Stress Induced Source of Phonon Bursts and Quasiparticle Poisoning

Permalink

https://escholarship.org/uc/item/9j33v426

Authors

Anthony-Petersen, Robin
Biekert, Andreas
Bunker, Raymond
et al.

Publication Date

2022-08-04

A Stress Induced Source of Phonon Bursts and Quasiparticle Poisoning

R. Anthony-Petersen,[1] A. Biekert,[1, 2] R. Bunker,[3] C.L. Chang,[4, 5, 6] Y.-Y. Chang,[1] L. Chaplinsky,[7]
E. Fascione,[8, 9] C.W. Fink,[1] M. Garcia-Sciveres,[2] R. Germond,[8, 9] W. Guo,[10, 11] S.A. Hertel,[7]
Z. Hong,[12] N.A. Kurinsky,[13] X. Li,[2] J. Lin,[1, 2] M. Lisovenko,[4] R. Mahapatra,[14] A.J. Mayer,[9]
D.N. McKinsey,[1, 2] S. Mehrotra,[1] N. Mirabolfathi,[14] B. Neblosky,[15] W.A. Page,[1, *] P.K. Patel,[7]
B. Penning,[16] H.D. Pinckney,[7] M. Platt,[14] M. Pyle,[1] M. Reed,[1] R.K. Romani,[1, *] H. Santana Queiroz,[1]
B. Sadoulet,[1] B. Serfass,[1] R. Smith,[1, 2] P. Sorensen,[2] B. Suerfu,[1, 2] A. Suzuki,[2] R. Underwood,[8]
V. Velan,[1, 2] G. Wang,[4] Y. Wang,[1, 2] S.L. Watkins,[1] M.R. Williams,[16] V. Yefremenko,[4] and J. Zhang[4]

[1]*Department of Physics, University of California, Berkeley, CA 94720, USA*
[2]*Lawrence Berkeley National Laboratory, Berkeley, CA 94720, USA*
[3]*Pacific Northwest National Laboratory, Richland, WA 99352, USA*
[4]*High Energy Physics Division, Argonne National Laboratory,*
9700 S. Cass Avenue, Argonne, Illinois 60439, USA
[5]*Department of Astronomy and Astrophysics, University of Chicago,*
5640 South Ellis Avenue, Chicago, Illinois 60637, USA
[6]*Kavli Institute for Cosmological Physics, University of Chicago,*
5640 South Ellis Avenue, Chicago, Illinois 60637, USA
[7]*Department of Physics, University of Massachusetts, Amherst, Massachusetts 01003, USA*
[8]*Department of Physics, Queen's University, Kingston, ON K7L 3N6, Canada*
[9]*TRIUMF, Vancouver, BC V6T 2A3, Canada*
[10]*Mechanical Engineering Department, FAMU-FSU College of Engineering,*
Florida State University, Tallahassee, Florida 32310, USA
[11]*National High Magnetic Field Laboratory, 1800 East Paul Dirac Drive, Tallahassee, Florida 32310, USA*
[12]*Department of Physics, University of Toronto, Toronto, ON M5S 1A7, Canada*
[13]*SLAC National Accelerator Laboratory/Kavli Institute for Particle*
Astrophysics and Cosmology, Menlo Park, California 94025, USA
[14]*Department of Physics and Astronomy, and the Mitchell Institute for Fundamental Physics and Astronomy,*
Texas A&M University, College Station, Texas 77843, USA
[15]*Department of Physics and Astronomy, Northwestern University, Evanston, IL 60208, USA*
[16]*University of Michigan, Randall Laboratory of Physics, Ann Arbor, MI 48109, USA*
(Dated: August 5, 2022)

The performance of superconducting qubits is degraded by a poorly characterized set of energy sources breaking the Cooper pairs responsible for superconductivity, creating a condition often called "quasiparticle poisoning". Recently, a superconductor with one of the lowest average quasiparticle densities ever measured exhibited quasiparticles primarily produced in bursts which decreased in rate with time after cooldown. Similarly, several cryogenic calorimeters used to search for dark matter have also observed an unknown source of low-energy phonon bursts that decrease in rate with time after cooldown. Here, we show that a silicon crystal glued to its holder exhibits a rate of low-energy phonon events that is more than two orders of magnitude larger than in a functionally identical crystal suspended from its holder in a low-stress state. The excess phonon event rate in the glued crystal decreases with time since cooldown, consistent with a source of phonon bursts which contributes to quasiparticle poisoning in quantum circuits and the low-energy events observed in cryogenic calorimeters. We argue that relaxation of thermally induced stress between the glue and crystal is the source of these events, and conclude that stress relaxation contributes to quasiparticle poisoning in superconducting qubits and the athermal phonon background in a broad class of rare-event searches.

I. INTRODUCTION

Coherence times are a key benchmark for the performance of superconducting qubits, a technology from which quantum computers may be constructed [1]. These times have improved by many orders of magnitude over the past two decades [2] but remain limited by mecha-

nisms capable of breaking Cooper pairs in the superconducting circuit, creating a condition often called quasiparticle poisoning [3–5]. Stray infrared radiation (IR) [6–8], environmental ionizing radiation [9–12], and resonant absorption of microwave photons [13, 14] have all been shown to create excess quasiparticles in superconducting quantum circuits. However, identification of the full set of poisoning mechanisms is yet incomplete, as suggested by other results in which efforts were made to shield and isolate superconducting circuits [10, 15].

Notably, a superconductor was recently shown to have

* These authors contributed equally to this work.;
rkromani@gmail.com

one of the lowest residual quasiparticle densities ever measured in a quantum circuit [15]. In this superconductor, two key behaviours were observed. First, the density of quasiparticles decreased as a function of time after the superconductor was cooled down. Second, the quasiparticles appeared in ms-long "bursts" which were short compared to the time between bursts. Together, these behaviors indicate that the cause of the quasiparticle background is unlikely to be fully explained by photons and ionizing radiation.

Similarly, multiple dark-matter experiments using cryogenic crystals observe excess low-energy (10–100 eV scale) events of an unknown origin [16–18]. Measurements suggest a background source that is nonionizing [19, 20] and which also decreases with time since cooldown [18, 19, 21, 22]; it is not well-explained by any known radiogenic or instrumental backgrounds.

The burst-like nature and variation in rate with time since cooldown suggest a common mechanism for these backgrounds and disfavor the sources of nonequilibrium quasiparticles thus far identified by the superconducting-qubit and dark-matter communities. For example, neither black-body IR that leaks from higher temperature stages [6, 7] nor the slow annihilation of quasiparticles near the superconducting gap [23] would create burst-like events. Short-lived radiogenic backgrounds could display a similar time dependence, but this dependence would not reset with thermal cycling. The lack of any ionization production in the germanium detectors used in Refs. [19, 20] further limits the viable hypotheses because both electronic and nuclear recoils produce observable ionization signals in this energy range [24].

The most probable hypothesis is that multi-atom lattice rearrangements, i.e. microfractures, causes these phonon bursts. The athermal phonons released in this process can break Cooper pairs in a qubit's superconducting films or be directly sensed in an athermal phonon sensor. If these microfractures are driven by stress caused by differential thermal contraction of a detector's materials or support structure—glue, clamps, metal films, etc.—this hypothesis also naturally explains the time variation since cooldown: the system is slowly releasing thermal stress and coming into equilibrium.

The CRESST dark-matter experiment has shown that stress-driven macroscopic fractures can cause phonon bursts [25]. Although the properties of their events—energy scale and time dependence—do not match the phonon bursts reported here, they provide an existence proof for stress-induced backgrounds in cryogenic devices.

An earlier iteration of the experiment clamped sapphire crystals with sapphire spheres, which tightened into the crystals at cryogenic temperatures and produced highly concentrated stress at the sphere/crystal contact points. Their detectors exhibited an excess rate of keV- to MeV-scale phonon bursts and macroscopic cracking at the clamp contact points. Redesigning the structural support to reduce the clamping force decreased this background by orders of magnitude [17, 25]. The observed bursts were found to be non-Poissonian, to not have noticeable time dependence in rate, and to occur at a much higher energy scale. These properties are incompatible with the low-energy background currently observed in cryogenic calorimeters and superconducting circuits; a different explanation is needed.

II. EXPERIMENTAL SETUP

We used two silicon crystals to study the effects of stress on the athermal phonon background: one mounted with a typical High Stress (HS) method and the other held with a new Low Stress (LS) method. The LS crystal was suspended by three sets of two 50 μm diameter aluminium wires (see Fig. 1, B), bonded to aluminium pads on the surface of the crystal and to a gold-plated copper mount which was attached rigidly to the cryogenic system. This reasonably represents a significantly lower-stress mounting scheme compared to glue- or clamp-based schemes and that it is naturally less susceptible to vibrations. The HS crystal was glued directly to the gold-plated copper mount using a thin layer of GE/IM7031 varnish covering the back side of the calorimeter, which contracts relative to the silicon while cooling [26], inducing stress in the crystal. We chose this configuration because it was straightforward to implement, and it is representative of the adhesive-based mounting schemes (e.g. vacuum grease [10, 15], silver epoxy [10]) often used to hold crystals that host quantum circuits. Additionally, the dark matter experiment that observed the largest low-energy excess [19] used epoxy, suggesting that glue may be a particularly effective source of stress-induced events.

Athermal phonon sensors optimized for high collection efficiency are a natural choice to study an anomalous phonon population capable of breaking Cooper pairs. We instrumented both the LS and HS crystals with functionally identical arrays of Quasiparticle-trap-assisted Electrothermal Feedback Transitions Edge Sensors (QETs) [27, 28], designed to be sensitive to athermal phonons with energies larger than the aluminium superconducting bandgap. The phonons are collected with $\mathcal{O}(10\%)$ efficiency and are read out with eV-scale energy resolution [29]. These sensors couple thin-film aluminium "fins," where athermal phonons are absorbed from the silicon crystal and converted into quasiparticles, with tungsten Transition Edge Sensors (TESs) that change resistance as they are heated by quasiparticle absorption. This readout scheme is broadly used in cryogenic calorimeters that search for low-energy signals from dark matter and neutrinos [16–18] and is optimally sensitive to any athermal phonons which may contribute to quasiparticle poisoning in quantum circuits.

Aside from their mounting schemes, the HS and LS calorimeters were intentionally constructed and operated in as similar a manner as possible. The phonon-sensor de-
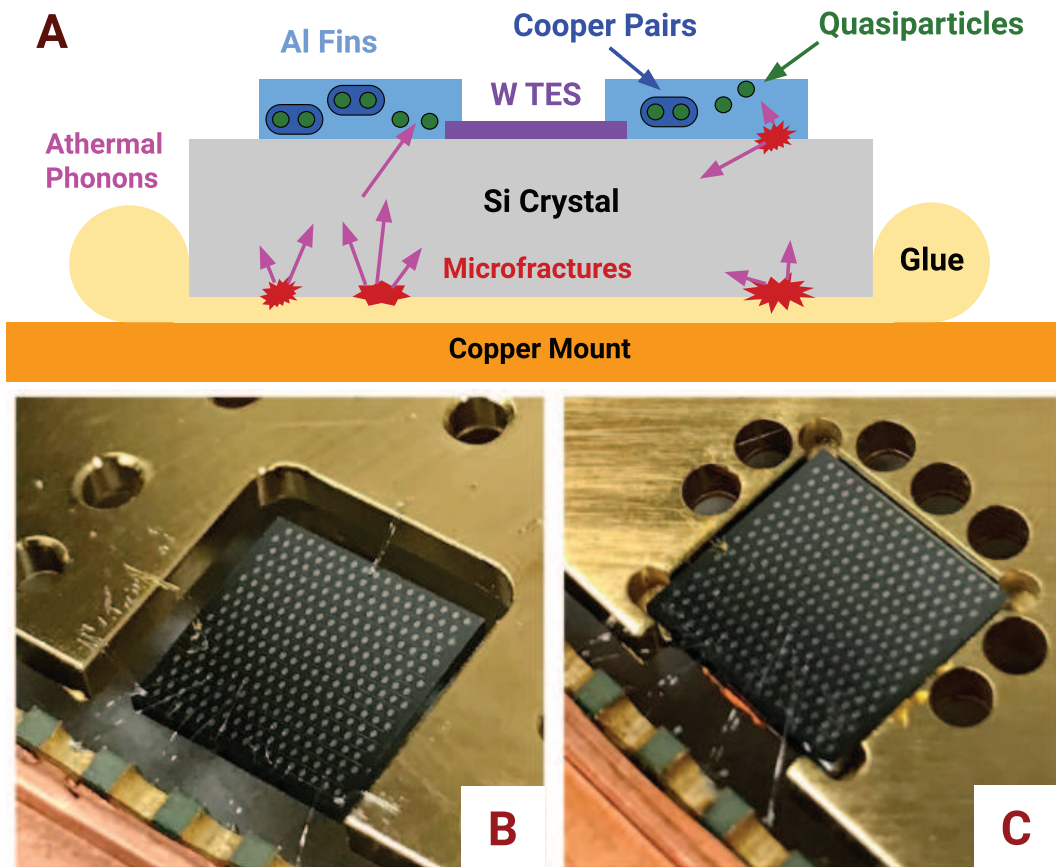
FIG. 1. **Schematic showing the orgin of microfracture events (Top, A) and photographs of the Low Stress (LS) silicon calorimeter (Bottom Left, B) and a functionally identical High Stress (HS) calorimeter (Bottom Right, C). (A)** The top schematic shows a silicon crystal glued to a copper mount (representative of **C**). Stress generated by thermal contraction relaxes via microfracture events (red), releasing energy as athermal phonons (pink) which break Cooper pairs (dark blue) in superconducting aluminium films (light blue) and create quasiparticles (green) that are read out with tungsten TESs (purple). **(B, C)** The calorimeters (grey) are 1 cm×1 cm by 1 mm thick. The LS calorimeter (left) is supported by three sets of two 50 μm diameter aluminium wire bonds, located at the back and the front of the left and right sides of the crystal. The HS calorimeter (right) is glued to a gold-plated copper mount using GE varnish. Both calorimeters are thermalized by several 25 μm diameter gold wire bonds (left side) and read out through 25 μm aluminium wire bonds (front). Athermal phonon readout sensors are visible as dots on the calorimeter tops.

signs are identical, and the sensors were fabricated onto (and the calorimeters later cut from) the same silicon wafer at Texas A&M University. The superconducting transition temperature (T_c) is an important indicator of performance for TES-based sensors [30]. We measured only a modest ∼20% difference between the TES transition temperatures for the two calorimeters (HS, 44.3 mK, LS, 53.0 mK), which also showed qualitatively similar sensor performance. These similarities suggest that we were largely successful in producing a matched calorimeter pair capable of isolating differences in background rates due to variation in structural support. Additionally, they were characterized together in a common optical cavity with a direct line of sight between the calorimeters and were read out using matching electronics, thereby minimizing operational differences. The dilution refrigerator in which this experiment was performed is located

in a basement lab at the University of California, Berkeley, where no special efforts were taken to minimize radioactive backgrounds.

III. DATA ANALYSIS

A. Measured Background

We observed a background event rate approximately two orders of magnitude larger in the HS device compared to the LS device. With the well understood electrothermal response of our phonon sensors, we identified the background as composed of individual events occurring in lengths of time shorter than the $\mathcal{O}(10~\mu\text{s})$ calorimeter response time, rather than as a continuous power source. The background spectra are shown in Fig.
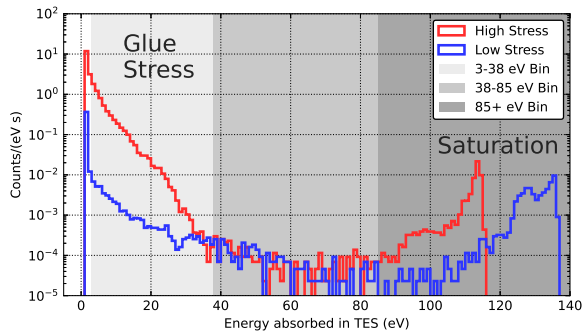
FIG. 2. **Background spectra of energy absorbed in TESs in High Stress and Low Stress calorimeters.** The histogram is divided into three regions: high energies associated with saturation (85+ eV), and two lower-energy bins (38–85 eV; 3–35 eV) where the backgrounds appear to be similar and different in the two calorimeters, respectively. These spectra are from a 12 hour dataset, the last of 7 datasets acquired (see Appendix E).
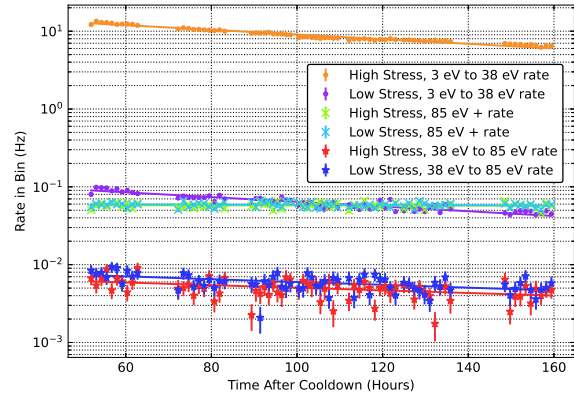

FIG. 3. **Time dependence of background rates in High Stress (light colors) and Low Stress (dark colors) calorimeters.** Rates are measured in three energy bins: 3–38 eV, 38–85 eV, and 85+ eV. Exponential fits are shown as solid lines.

2. We report the energy of a given event as the energy absorbed in the TES (which is invariant to small changes in film properties, as described in Sec. V D). Note that at high energies the calorimeters saturate such that all very energetic events appear in the energy range 85–170 eV. The exact energy scale and shape of the saturation depends on tungsten film properties, which were observed to vary between the two devices (see Sec. V A), leading to the differences in saturation observed between the two devices.

The background was divided into three energy bins for further analysis. The highest-energy events (85+ eV) with a saturated calorimeter response were binned together. In the range 38–85 eV, the backgrounds observed in HS and LS were similar; we therefore grouped them together into one bin. In the lowest-energy bin (3–38 eV), the backgrounds observed in the HS and LS calorimeters appear to substantially differ.

B. Time Dependence of Background Rates

To study the time dependence of these backgrounds, ∼80 hours of data were taken over a 5 d period, starting approximately 3 d after starting the cooldown of the calorimeters. During this period, the rate in each of the three energy bins (see Fig. 2) was measured 70× for each calorimeter in ∼1 hour time bins (see Table IV).

As shown in Fig. 3, the rates in both the 3–38 and 38–85 eV bins decreased with time, whereas the rates in the highest-energy bin (85+ eV) were constant (consistent with muons and other high-energy backgrounds). An exponential was fit to each time-dependent rate to estimate the relevant timescale; the results are summarized in Table I. We find that the 3–38 and 30–85 eV rates decreased with a time constant of 6–10 d, broadly con-

sistent with the quasiparticle measurements in Ref. [15] and calorimetric results in Refs. [19, 21, 22]. We did not test whether the observed rates changed after thermal cycling, and plan to study this in future work.

In the lowest-energy bin in the HS calorimeter, a single exponential does not sufficiently describe the time-dependent rate ($\chi^2/(\mathrm{dof}) = 4192/68$). This bin is especially well-measured because it contains 2–3 orders of magnitude more events than any of the other bins. There may be similar deviations from our exponential model in the other time-series data that cannot be detected due to insufficient statistics. A sum of exponentials or a power law (as described in Ref. [15]) may be a more appropriate fit to the data.

As the HS and LS calorimeters were functionally identical aside from their mounting method, we attribute the difference in their 3–38 eV backgrounds as due to stress from the GE varnish contracting relative to the HS crystal. When this stress relaxes in the form of a microfracture, many eV-scale bonds are broken effectively instantaneously with respect to the calorimeter response, releasing phonon energy which our sensors read out as a single event. The relatively short decay time (6–10 d) indicates that non-artificially activated radioactive backgrounds cannot be responsible for the observed events. The scintillation mechanism suggested in Ref. [31] cannot compose a large fraction of the observed background because it decreased with time and was not coincident between our two detectors, which were closely co-located in the same optical cavity. IR photon backgrounds would not decrease with time given constant cryogenic performance (as was observed), would not be concentrated into events with tens of eV deposited within the ∼ 10 μs calorimeter response time, and would be expected to be coincident between the two detectors.

Within the 38–85 eV range, the event rate increased quasi-exponentially with decreasing energy and decreased with time, similar to the stress-relaxation process observed at lower energies in the HS calorimeter. However, the magnitude, spectral shape, and time dependence of the 38–85 eV rate were consistent in both devices (see Table I), indicating that mount-related stress may not be the cause of the background in this energy range. We hypothesize that stress in the QET thin films may be responsible. As the crystal, films, and photolithographically etched design are all essentially identical between the two devices, this background (if present) should be very similar between the two calorimeters. Both differential thermal contraction between the crystal and films during cooldown and relative strain created during film deposition are natural sources of such stress.

To demonstrate the plausibility of film stresses as a source of background events, we briefly sketch the physics of an aluminium film that becomes stressed when cooling from room temperature to close to absolute zero. Relative to a silicon substrate, aluminium will contract by a factor of about 4×10^{-3} [32], yielding an energy density of ~ 5 MeV/μm^3. Given the 600 nm aluminium film thickness, the stress energy per unit area is of order 35 meV/Å^2 at the Al/Si interface. This is comparable to the 40–100 meV/Å^2 fracture energy density thresholds reported in Ref. [33], suggesting that film microfractures via this mechanism are plausible.

C. Inferred Residual Quasiparticle Density Scales

To contextualize our observation of stress-induced athermal phonons for the superconducting qubit community, we estimate reduced quasiparticle densities x_{qp} based on simulations described in Sec. V F and Appendix C. We simulate the quasiparticles produced by our observed stress-induced phonon events as well as high-energy backgrounds (muons, etc.) in two representative quasiparticle dynamics limits: the recombination-dominated qubit in Ref. [11] and the trapping-dominated superconductor in Ref. [15]. We emphasize that these estimates merely indicate that the properties and approximate scale of the quasiparticle densities simulated with our stress-induced events are in general agreement with the densities observed in previous experiments. Exact quasiparticle densities may differ significantly from our estimates because of the inherent variation among setups (glue type, superconductor geometry, etc.),

In the case of the qubit, we find that our stress-induced background would produce a reduced quasiparticle density of $x_{qp} \approx 5.0 \times 10^{-8}$, while high-energy backgrounds should induce $x_{qp} \approx 1.5 \times 10^{-8}$. The latter is in general agreement with the lower bound of $x_{qp} \geq 7 \times 10^{-9}$ estimated in Ref. [11] for high-energy backgrounds. For the system in Ref. [15], we find that our stress events induce $x_{qp} \approx 2.8 \times 10^{-11}$, while high-energy backgrounds induce $x_{qp} \approx 3.3 \times 10^{-10}$.

These estimates suggest that in the case of recombination-dominated systems similar to Ref. [11], stress backgrounds may already cause quasiparticle densities comparable to or greater than those created by high-energy backgrounds. Running qubits in low-background, underground environments [10] would presumably only increase the relative importance of stress-induced backgrounds. The striking similarities (time dependence of rate, etc.) between the residual quasiparticle densities observed in Ref. [15] and our athermal phonon population observations strongly suggest that stress-induced phonons were the primary cause of their quasiparticle bursts. The difference between our simulated quasiparticle densities and their observations suggests that stress events occurred at a higher rate or energy scale in their system.

IV. CONCLUSION

We observed that mounting a cryogenically cooled silicon crystal with GE varnish leads to a large rate of athermal phonon events with energies in the range of 10s–100s of eV per event. The mounting of crystals with other glue-like substances—e.g., vacuum grease [15] or epoxy [10]—likely also results in a population of athermal phonons. Experimenters constructing quasiparticle-sensitive quantum circuits or low-threshold calorimeters on cryogenic crystals should therefore consider alternative mounting techniques (such as suspending crystals from wire bonds) that avoid use of adhesives.

More broadly, experiments which are sensitive to athermal phonon backgrounds may be sensitive to stress in their crystals from a variety of mechanisms. In addition to adhesive-based mounting schemes, using clamps to hold crystals can result in excess event rates [25]. Based on our results, we also hypothesize that stress between a device's crystal substrate and thin films may be a source of stress-induced events (see Sec. III B). A systematic program of stress reduction may substantially decrease both the low-energy excesses currently observed in cryogenic calorimeters used to search for dark matter and the time-dependent component of the quasiparticle poisoning problem in quantum circuits.

V. METHODS

A. Calorimeter Construction

In our calorimeters (see Fig. 1), phonons from the silicon crystal are absorbed by aluminium fins patterned onto the crystal's surface. These phonons break Cooper pairs and create quasiparticles, which diffuse to and are absorbed by tungsten TESs coupled to the aluminium fins. When heated by quasiparticle thermalization, the current through a voltage-biased TES changes as the resistance changes. This change in current can be read out

using SQUID electronics. A small gold pad on the silicon surface was connected to the thermal bath via a gold wire bond, thus removing thermal phonons from the crystal.

Our calorimeters were fabricated from a single 1 mm thick, 100 mm diameter polished high-purity wafer (Float Zone intrinsic silicon, >10 kOhm/square). Tungsten, aluminium, and gold films were deposited onto the crystal surface, and then photolithographically etched into the desired shapes.

The T_cs of the HS and LS devices were measured to be 44.3 and 53.0 mK, respectively. The fraction of the surface area of the calorimeters (including sidewalls and bottoms) covered by "active" aluminium fins (which collect athermal phonons into TESs) and tungsten TESs (which collect sub-gap phonons) were 2.8% and 0.29%. The "passive" areal fractions of aluminium, tungsten, and gold were 3.3%, 0.29%, and 0.037%, respectively. By design, these coverage fractions were similar to the calorimeter used in Ref. [16]. We note that the fraction of "passive" aluminium and tungsten includes approximately half of the total number of QETs, which were not read out due to broken wire bonds. The broken readout channel was the same for both calorimeters.

B. Cryogenic Configuration

The HS and LS calorimeters were run inside a Cryoconcept HEXADRY UQT-B 200 dry (pulse tube based) dilution refrigerator. The refrigerator was located in a subbasement lab at the University of California, Berkeley, with minimal overburden and no radiation shielding (lead, etc.). No special radiopurity precautions were undertaken.

The configuration of the refrigerator and pulse tube cooler were optimized to transmit minimal vibrations from the pulse tube to the cold stages of the refrigerator. Further, both the HS and LS mounting schemes are relatively insusceptible to vibrations. We operated the refrigerator in a "pulse tube off" configuration for short periods of time (up to 15 min) and did not measure any significant difference in noise, performance, or background (vs. pulse tube on) for either the HS or LS calorimeter. All data presented in this paper were recorded with the pulse tube on and with a stable refrigerator base temperature < 10 mK. We have also studied a low-stress "resting" configuration in which the calorimeter was sitting directly on a copper surface without being glued down; these devices were extremely susceptible to pulse-tube vibrations.

The HS and LS calorimeters were located inside the same copper optical cavity, with a direct line of sight between them. The printed circuit boards used to read out the calorimetry signals were also located in this optical cavity, presumably leading to a subdominant scintillation background as described in Ref. [31]. This cavity was held at the temperature of the mixing chamber ($\sim$10 mK) and was sealed with copper tape to increase light tightness. The mixing chamber and the optical cavity were located inside the refrigerator's still thermal shield ($\sim$1 K), which was in turn located inside 4 K and 50 K shields sealed inside a 300 K vacuum can. An external mu-metal shield was used to reduce internal magnetic fields.

C. Readout Signal Chain

The HS and LS calorimeters were read out using standard TES readout techniques (see, e.g., Ref. [27]). The current flowing through the TESs was read out using a SQUID amplifier on the 100 mK cold-plate stage of the dilution refrigerator. This SQUID was operated in a feedback mode and was controlled by room-temperature electronics. Data were collected continuously with a National Instruments PCIe-6376 DAQ operating at 1.25 MHz.

D. Data Collection and Energy Measurement

Approximately 80 hours of data were collected in 7 datasets, summarized in Table IV. For both the HS and LS calorimeters, each dataset was recorded as a continuous stream, and a threshold-based event selection was carried out with offline software. Pulses in the continuous data stream were found using an optimal filtering approach, and 20 ms traces (symmetric around the pulse) were recorded for each event. The resulting set of triggered events were then processed using an optimal filtering algorithm to measure pulse heights.

Thanks to the well understood electrothermal feedback mechanism in TESs [27], we can directly infer the energy absorbed in a TES from the size of a pulse. After determining the pulse height in units of current using the optimal filtering algorithm, we calculated the power absorbed in the TES in the infinite loop gain limit as

$$P_{abs} = \delta I \frac{\partial P}{\partial I}(\omega = 0) = \delta I (2 I_{TES} R_{Load} - V_{bias}). \quad (1)$$

We multiplied this peak power by the integral of the pulse-fitting template (in units of time) to find the energy associated with the pulse. This method of calculating the energy absorbed in the TES is in general insensitive to the exact characteristics of the TES film (given films with similar α which are significantly colder than T_c, as was the case for our calorimeters). Note that the energy measured with this approach corresponds to the energy absorbed in the TES, rather than the energy deposited in the phonon system. As described in Appendix B, the latter can be estimated by assuming a phonon collection efficiency of 12.5%.

In the case of saturation, the temperature of the TES rises significantly above T_c and the electrothermal feedback mechanism fails to completely capture the energy absorbed in the TES. Therefore, the energy of saturated pulses measured using this approach will be underestimated. The energy at which this saturation takes place

depends on the T_c of the film, among other factors, leading to the variation in saturation energy seen in Fig. 2.

Because we did not directly calibrate the phonon collection efficiency, we report energy as absorbed in the TESs rather than energy deposited in the calorimeter (aside from the estimates in Appendix B). Given the phonon collection efficiencies observed in similar calorimeters [29], we can safely conclude that the events we observe are relevent to the observed low energy excess. Our analysis and conclusions are otherwise insensitive to the exact energy that the observed events deposit in the calorimeter.

E. Data Quality Cuts

To ensure a consistent detector response, only the events passing three sets of data-quality cuts were considered for analysis. Events were required to pass

- a *baseline cut* requiring the magnitude of the pre-pulse baseline to be in a range associated with consistent detector response,

- a *slope cut* requiring the slope of the baseline before and after a pulse to be consistent with steady-state detector operation, and

- a *chi-squared cut* requiring the shape of the pulse to be consistent with a representative pulse template.

These cuts were designed to pass a large fraction of events. Passage fractions are summarized in Tables V and VI.

Pulses larger than a threshold associated with saturation failed to pass both the slope and chi-squared cuts, even for pulses associated with the expected response of the device. All such saturated pulses were therefore set to pass and were thus included in our reported (85+ eV) event rates. These pulses are outside of the main region of interest for this analysis.

Cut passage fraction as a function of time was monitored by finding the passage fraction of randomly acquired traces as a function of time. Our reported event rates have been corrected by this measured passage fraction to account for cut efficiency. Note that the passage fraction did not significantly vary over time and was never less than 0.85, indicating that cut-efficiency time dependence cannot be the source of the rate variation described in Sec. III B.

F. Quasiparticle Density Simulations

For our quasiparticle density estimates, we use a zero dimensional model in which the quasiparticle dynamics for the reduced quasiparticle density, $x_{qp} = n_{qp}/n_{cp}$, are governed by

$$\frac{dx_{qp}(t)}{dt} = -rx_{qp}(t)^2 - sx_{qp}(t) + g(t), \qquad (2)$$

where n_{qp} and n_{cp} are the number densities of quasiparticles and Cooper pairs, respectively, $r \approx (20\,\text{ns})^{-1}$ is the constant associated with recombination in aluminium [34], s is the trapping rate in a given system, and g is the quasiparticle generation rate. We approximate g by $g_0\delta(t - t_0)$, where

$$g_0 = \frac{Ef}{2\Delta A d n_{cp}}, \qquad (3)$$

E is the phonon energy of the event in a device substrate, $f \approx 0.5$ [35] is the collection efficiency of phonon event energy into quasiparticles, A and d are the area and thickness of the superconductor (qubits and ground plane combined), respectively, $\Delta \approx 180\mu\text{eV}$ is the superconducting bandgap of aluminium, and $n_{cp} \approx 4 \times 10^6 \mu\text{m}^{-3}$ is the Cooper pair density in aluminium.

We estimate x_{qp} for two systems. One system is recombination-limited (i.e., $s \approx 0$, modeled after the device in Ref. [11]), with $\sim 100\%$ superconductor surface coverage and a superconductor thickness of 200 nm. In the other system, dominated by trapping (modeled after the device in Ref. [15]), we assume a 20 % coverage fraction, a 35 nm thick superconductor, and $s = 8.0$ kHz. The properties of the two systems are summarized in Table III.

In both systems, we use the actual measured behavior of our HS calorimeter to model g_0 and t_0 and thus construct $g(t)$ and $x_{qp}(t)$. For events under the saturation threshold, we use event energies and timing without modification. For saturated events, in simulations that include high-energy backgrounds, we assign an energy of 100 keV (similar to Ref. [34]); whereas, these events are assigned 0 eV for simulations without high-energy backgrounds. The datasets with zero energy from saturated events are designed to simulate the performance of a qubit operated in a well-shielded setup, such as an underground laboratory with good radiopurity controls where high-energy backgrounds would be greatly reduced (as suggested in Ref. [10]).

We numerically simulate $x_{qp}(t)$ with the constructed $g(t)$ in 25 μs time steps. After discarding an initial period, during which the simulation equilibrated, the simulated $x_{qp}(t)$ was plotted (see Fig. 5) and time averages were taken (see Table II). Simulations were performed for each system—recombination and trapping dominated—with only high-energy backgrounds, with only stress backgrounds, and with both backgrounds. The results are summarized in Sec. III C and further discussed in Appendix C.

performed critical precursor work on resting calorimeters. The calorimeters used in this study were designed by C.F. and were fabricated at Texas A&M University by M. Platt. S.M., W.A.P., M.R., and R.K.R. developed the low-stress hanging technique, and M.R. and R.K.R. assembled the LS and HS calorimeters. DAQ and other software tools used in this analysis were designed by C.F., W.A.P., B. Serfass, B. Suerfu, and S.L.W. The main data analysis was undertaken by R.K.R. All authors read and approved the manuscript, which was written primarily by R.B., M. Pyle and R.K.R.

Appendix A: Summary of Fits to Background Rate vs. Time Data

In Table I, we summarize the fits to the data describing the background rate as a function of time.

Appendix B: Comparison with Other Calorimetric Experiments

For comparison, we show the low-energy spectra measured with our HS and LS devices alongside the spectra observed in the CPD [16] and CRESST-III [17] calorimeters in Fig. 4. This comparison assumes a phonon collection efficiency of 12.5% in the HS and LS calorimeters, consistent with the observed collection efficiencies for devices of this type within $\mathcal{O}(2)$ [16]. The low-energy excesses in all of these calorimeters were found to vary with time constants in the range of weeks [21, 22]. We hypothesize that varying levels of stress, either in the thin films (see section III B) or as a result of the crystal mounting schemes, are responsible for some of the discrepancy in background rates. Note that the elevated background observed in the HS and LS calorimeters cannot be entirely due to a UC Berkeley cryostat-specific effect (e.g., larger environmental backgrounds), because the CPD detector from Ref. [16] was operated in the UC Berkeley cryostat and measured a background consistent with the published spectrum to within a factor of two.
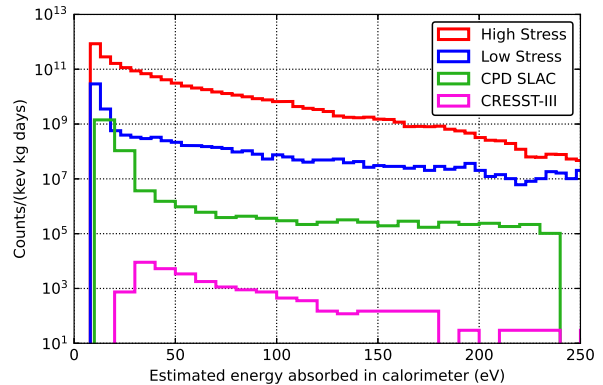
FIG. 4. **Comparison to CPD and CRESST.** Spectra of events in HS and LS calorimeters, compared to those measured with the CRESST-III detector [17] and by SuperCDMS in the CPD detector at SLAC [16]. Data are from the last of seven datasets taken. The energy in the HS and LS calorimeters are estimated assuming a phonon collection efficiency of 12.5%, and therefore differ by a constant factor from the spectra in Fig. 2.

Appendix C: Estimating Quasiparticle Densities for Representative Quantum Systems

Athermal phonons incident on a superconductor can break Cooper pairs in the superconductor, creating quasiparticles which can cause decoherence of superconducting qubits. The impact of "high energy" backgrounds on quantum circuit performance has recently been the subject of significant study [10, 11, 34]. In this section, we comment on the importance of such high-energy backgrounds relative to stress-induced backgrounds.

To this end, we separate the background observed in our calorimeters into two regions: the first between 3 and 85 eV (the two lowest-energy bins in Fig. 2), and the second above 85 eV where the response of the detector saturates such that the energy deposited in the detector cannot be accurately reconstructed. We associate the first region with stress-related events (as argued in Sec. III B) and the second region with cosmic-ray muons, high-energy gammas, neutrons, alphas, etc. interacting with the calorimeter. As we cannot accurately reconstruct the energy of these saturated events, we assume that each deposits 100 keV of energy in the phonon system, corresponding approximately to the energy deposited by a minimum ionizing muon [36] and similar to the average energy in Ref. [34].

In the simplest terms, we can compare the relative powers of the high-energy and stress-induced backgrounds. For example, in our first dataset, we see a rate of approximately 672 eV/s of stress events in the HS calorimeter, 10.9 eV/s in the LS calorimeter, and 5.8 keV/s of high-energy backgrounds in either calorimeter—summing the energies observed directly in

TABLE I. **High and Low Stress calorimeter rates and their time dependence.**

Stress, Bin	Relative Rate[a]	Decay Const. (1/d)	Fit τ (d)	χ^2/(dof)
High, 3–38 eV	1.000 ± 0.026	0.1659 ± 0.0039	6.03 ± 0.14	4192/68
High, 38–85 eV	$(4.93 \pm 0.58) \times 10^{-4}$	0.093 ± 0.023	10.8 ± 2.7	93.5/68
High, 85+ eV	$(4.83 \pm 0.20) \times 10^{-3}$	0.0017 ± 0.0070		90.7/68
Low, 3–38 eV	$(7.10 \pm 0.31) \times 10^{-3}$	0.1678 ± 0.0082	5.96 ± 0.29	124.8/68
Low, 38–85 eV	$(5.92 \pm 0.59) \times 10^{-4}$	0.100 ± 0.020	9.97 ± 1.96	83.1/68
Low, 85+ eV	$(4.96 \pm 0.19) \times 10^{-3}$	0.0076 ± 0.0062		70.2/68

[a] Note: Uncertainties are 1σ. Fit τ is derived from the fit Decay Constant, and are not reported for the high energy bins for either calorimeter, as the fit decay constants are consistent with being flat with respect to time

[a] Fit rate relative to the fit rate in the high stress 3–38 eV bin (60 hours after cooldown).

the case of stress backgrounds and assuming 100 keV per saturated event in the case of high-energy backgrounds. In radiopure underground cryostats, as suggested in Ref. [10], the high-energy background power may be reduced by as much as a factor of 10^4, implying that stress-induced backgrounds may completely dominate the phonon-background power in such systems.

In many quantum circuits, the average quasiparticle density depends not only on the power of phonons incident on the superconducting elements but also on the average energy of the phonon events. Inspecting Eq. 2 in Sec. V F, we note that if the system is dominated by recombination (i.e., s is small, as in many quantum circuits [11]) and g is not constant with time, as is the case for both high-energy and stress-related quasiparticle creation, then the time-averaged quasiparticle density will in general be smaller for infrequent high-energy events than for frequent low-energy events, even if both backgrounds have similar powers. Dense quasiparticle populations created by infrequent high-energy events will recombine more quickly than more diffuse quasiparticle populations created by frequent low-energy events.

We simulated the time-dependent quasiparticle density in two cases: a recombination-limited superconductor modeled after Ref. [11] and a trapping-dominated superconductor based on Ref. [15] (as discussed in Sec. III C and Sec. V F). In both cases, we simulate the quasiparticle densities based on measured phonon event energies and timing in our HS calorimeter, assigning a phonon energy of 100 keV for saturated events. Figure 5 shows the simulated quasiparticle densities.

In the recombination-dominated case (i.e., insignificant quasiparticle trapping), we simulate a time-averaged value of $x_{qp} \approx 4.1 \times 10^{-8}$ due to stress events only and 5.0×10^{-8} if energy from high-energy backgrounds is included. The simulated reduced quasiparticle density due to high-energy backgrounds alone is 1.5×10^{-8}, which is comparable to the $x_{qp} \geq 7 \times 10^{-9}$ lower bound estimated in Ref. [11] for background radiation. While it is notable that the stress-induced and high-energy contributions to x_{qp} are comparable in this recombination-dominated case, this will not be generally true; stress-induced events may occur in different systems with significantly different rates or energy scales that depend on

details of the experimental setup.

Multiple works [34, 37] have suggested using quasiparticle traps to suppress the time-averaged residual quasiparticle density. We simulate such a system (based on Ref. [15]) with the same event-rate assumptions as for the recombination-dominated case and estimate $x_{qp} = 3.6 \times 10^{-10}$ if high-energy backgrounds are included and 2.8×10^{-11} with only stress events included, approximately three orders of magnitude lower than measured in Ref. [15]. However, if we increase the average energy per stress event by a factor of 10^3, or equivalently increase the rate density of events by a factor of 10^3 and assume energy is much more locally absorbed, we recover $x_{qp} \approx 2.8 \times 10^{-8}$ both with and without high-energy backgrounds (as observed shortly after cooldown in Ref. [15]). This increased energy scale ($E \approx 10$ keV) is still lower than the scale of events observed by CRESST [25], suggesting that some combination of increases in rate and energy scale plausibly explains the time-varying quasiparticle density observed in Ref. [15].

Previously discussed mitigation techniques include operating radiopure quantum circuits in low-background environments [10, 11] (which would not reduce the stress-induced phonon background) and using phonon sinks to reduce the background athermal phonon populations [34]. Phonon sinks would reduce the effects of the stress-induced phonon background if the phonons are generated by, e.g., glue-crystal microfractures. However, phonon sinks would not significantly mitigate the effects of film-crystal microfractures, e.g., between the crystal and superconducting qubit thin films. In the latter case, energy would presumably be efficiently transferred to the quasiparticle system of the qubit without involving significant crystal-scale phonon propagation. As we have shown, trapping quasiparticles within the qubit [34, 37] would somewhat mitigate the effects of stress-induced athermal phonons, but a resolution of the underlying athermal phonon problem is needed to achieve thermal densities of quasiparticles.

In summary, our simulations indicate that in the case of the recombination-dominated qubit, stress and high-energy backgrounds plausibly contribute about equally to quasiparticle poisoning, while experimental evidence [15] indicates that the quasiparticle density is dominated by
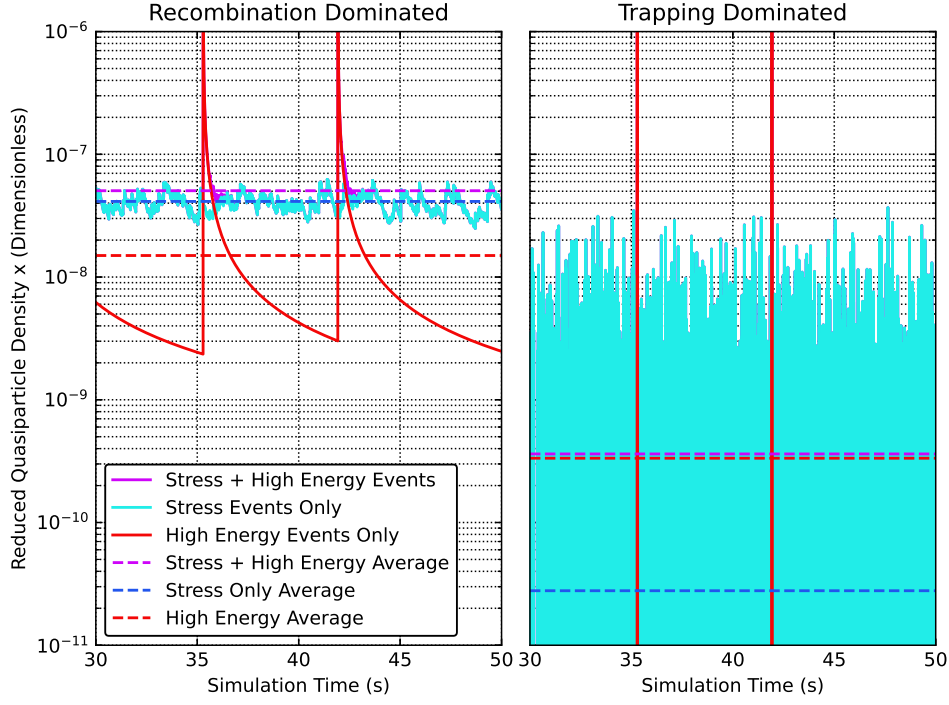
FIG. 5. **Simulated Reduced Quasiparticle Density x_{qp} in Recombination- and Trapping-Dominated Systems vs. Time.** Simulations are based on observed events in the high stress calorimeter (see Appendix C for details). Note that in the trapping-dominated simulation (right), due to the fast trapping timescale both curves are only on scale for a short length of time after each event; the average value of x_{qp} is well below 10^{-9}. The recombination-dominated qubit was modeled after Ref. [11] and the trapping-dominating superconductor was modeled after Ref. [15]. Dotted lines are time averages.

TABLE II. **Quasiparticle Background Simulation Results.**

	Average Power	Recombination Dominated x_{qp} [a]	Trapping Dominated x_{qp} [b]
High-energy Backgrounds	5.8 keV/s	1.5×10^{-8}	3.3×10^{-10}
Stress-induced Backgrounds	672 eV/s	4.1×10^{-8}	2.7×10^{-11}
Stress + High Energy	6.5 keV/s	5.0×10^{-8}	3.6×10^{-10}

[a] Modeled after a recombination-dominated qubit in Ref. [11].
[b] Modeled after a trapping-dominated superconductor in Ref. [15].
  Modeled x_{qp} and measured powers derived from HS dataset 1.

TABLE III. **Superconductor Properties used in Residual Quasiparticle Density Simulations.**

	Recombination-Dominated Superconductor [a]	Trapping-Dominated Superconductor [b]
Thickness	200 nm	35 nm
Superconductor Coverage Fraction	100 %	40%
Recombination Time Constant r	$(20 \text{ ns})^{-1}$	$(20 \text{ ns})^{-1}$
Trapping Rate s	0 Hz	8 kHz
Phonon Collection Efficiency	50%	50%

[a] Modeled after a recombination-dominated qubit in Ref. [11].
[b] Modeled after a trapping-dominated superconductor in Ref. [15].
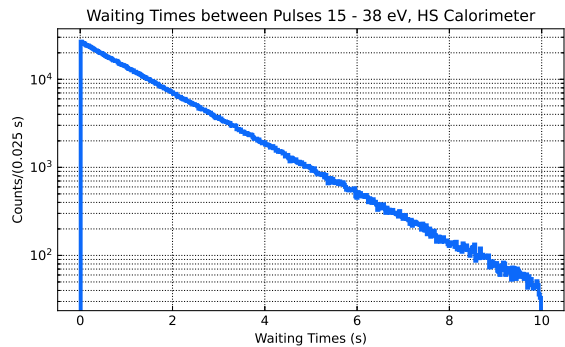
FIG. 6. **Waiting Time Distribution in the High Stress Calorimeter.** Time until another event ("waiting time") in the 15–38 eV energy range in a high stress calorimeter. We expect events in this energy range to be primarily composed of microfracture events. The data are well-described by a Poissionian model, in contrast to those in Ref. [25].

stress-induced quasiparticles in the trapping-dominated superconductor. In either case, the rate and energy scale of stress-induced events will presumably vary from experiment to experiment, either increasing or decreasing the relative importance of this background.

The simulated residual quasiparticle densities are summarized in Table II, while the properties of the superconductors modeled in our simulations are listed in Table III.

Appendix D: Waiting Time Distribution

In Ref. [25], the distribution of waiting times between events was studied and used to argue that a fracture-like process was responsible for the observed excess background. Shown in Fig. 6, we performed a similar study of the distribution of waiting times in our HS calorimeter for low-energy events, which we argue are largely microfracture events.

The distribution of waiting times for our microfracture events does not agree with the deviations to the Possionian model presented in Ref. [25]. Notably, we are observing a fracture process taking place at an energy scale around three orders of magnitude lower than observed in the CRESST calorimeters. Presumably, even very similar fracture mechanisms may manifest differently at such different energy scales.

Appendix E: Summary of Datasets Taken

In Table IV, we summarize the various datasets that were taken, specifying the start time, end time, and duration of each dataset.

Appendix F: Summary of Cut Passage Fraction

In Tables V and VI, we summarize the passage fractions of our data quality cuts, applied to the randomly triggered data and the threshold triggered data, respectively.

[1] P. Krantz, M. Kjaergaard, F. Yan, T. P. Orlando, S. Gustavsson, and W. D. Oliver, A quantum engineer's guide to superconducting qubits, Appl. Phys. Rev. **6**, 021318 (2019).

[2] W. D. Oliver and P. B. Welander, Materials in superconducting quantum bits, MRS Bull. **38**, 816 (2013).

[3] J. Aumentado, M. W. Keller, J. M. Martinis, and M. H. Devoret, Nonequilibrium quasiparticles and 2e periodicity in single-Cooper-pair transistors, Phys. Rev. Lett. **92**, 066802 (2004).

[4] J. M. Martinis, M. Ansmann, and J. Aumentado, Energy decay in superconducting Josephson-junction qubits from nonequilibrium quasiparticle excitations, Phys. Rev. Lett. **103**, 097002 (2009).

[5] K. Serniak, M. Hays, G. de Lange, S. Diamond, S. Shankar, L. D. Burkhart, L. Frunzio, M. Houzet, and M. H. Devoret, Hot non-equilibrium quasiparticles in transmon qubits, Phys. Rev. Lett. **121**, 157701 (2018).

[6] A. D. Córcoles, J. M. Chow, J. M. Gambetta, C. Rigetti, J. R. Rozen, G. A. Keefe, M. B. Rothwell, M. B. Ketchen, and M. Steffen, Protecting superconducting qubits from radiation, Appl. Phys. Lett. **99**, 181906 (2011).

[7] R. Barends, J. Wenner, M. Lenander, Y. Chen, R. C. Bialczak, J. Kelly, E. Lucero, P. O'Malley, M. Mariantoni, D. Sank, et al., Minimizing quasiparticle generation from stray infrared light in superconducting quantum circuits, Appl. Phys. Lett. **99**, 113507 (2011).

[8] C.-H. Liu, D. C. Harrison, S. Patel, C. D. Wilen, O. Rafferty, A. Shearrow, A. Ballard, V. Iaia, J. Ku, B. L. T. Plourde, et al., Quasiparticle poisoning of superconducting qubits from resonant absorption of pair-breaking photons (2022), arXiv:2203.06577 [quant-ph].

[9] M. McEwen, L. Faoro, K. Arya, A. Dunsworth, T. Huang, S. Kim, B. Burkett, A. Fowler, F. Arute, J. C. Bardin, et al., Resolving catastrophic error bursts from cosmic rays in large arrays of superconducting qubits, Nature Phys. **18**, 107 (2022).

[10] L. Cardani, F. Valenti, N. Casali, G. Catelani, T. Charpentier, M. Clemenza, I. Colantoni, A. Cruciani, L. Gironi, L. Grünhaupt, et al., Reducing the impact of radioactivity on quantum circuits in a deep-underground facility, Nature Commun. **12**, 2733 (2021).

TABLE IV. **Table of datasets taken.**

Dataset Number	Start Date	Start Time (UTC)	Length (Hours)
1	2022-05-03	21:54:54	12.06
2	2022-05-04	18:15:33	12.06
3	2022-05-05	11:23:22	10.06
4	2022-05-05	22:25:41	10.06
5	2022-05-06	10:08:08	12.07
6	2022-05-06	22:58:07	12.07
7	2022-05-07	22:32:50	12.07

TABLE V. Summary of the passage fraction of randomly selected events in each of the 7 data taking periods, showing passage fraction for the baseline, slope, and χ^2 cuts. These events do not necessarily contain a pulse. These randomly selected events allow for us to study the passage fraction of infinitesimally small events.

Dataset No., Stress State	Baseline	Slope (Sequential)	Slope (Total)	χ^2 (Sequential)	χ^2 (Total)	Total Passage
1, Low Stress	0.964	1.00	0.964	0.973	0.973	0.939
2, Low Stress	0.966	1.00	0.966	0.984	0.984	0.951
3, Low Stress	0.962	1.00	0.965	0.995	0.995	0.960
4, Low Stress	0.969	1.00	0.969	0.981	0.981	0.951
5, Low Stress	0.965	1.00	0.965	0.979	0.978	0.944
6, Low Stress	0.970	1.00	0.970	0.985	0.985	0.956
7, Low Stress	0.968	1.00	0.969	0.983	0.983	0.951
1, High Stress	0.952	1.00	0.952	0.970	0.970	0.923
2, High Stress	0.952	1.00	0.946	0.977	0.977	0.930
3, High Stress	0.940	1.00	0.956	0.970	0.970	0.927
4, High Stress	0.959	1.00	0.959	0.937	0.937	0.898
5, High Stress	0.959	1.00	0.959	0.978	0.977	0.937
6, High Stress	0.960	1.00	0.960	0.979	0.979	0.939
7, High Stress	0.959	1.00	0.963	0.982	0.982	0.936
1, High + Low Stress						0.869
2, High + Low Stress						0.889
3, High + Low Stress						0.892
4, High + Low Stress						0.857
5, High + Low Stress						0.888
6, High + Low Stress						0.901
7, High + Low Stress						0.893

Cuts are applied sequentially. Sequential passage is the fraction of events that passed the previous cut which also pass this cut, total passage is the fraction of all events that pass this cut.
High + Low Stress total passage fractions show the passage fraction for the combined total high and low stress cuts.

[11] A. Vepsäläinen, A. H. Karamlou, J. L. Orrell, A. S. Dogra, B. Loer, F. Vasconcelos, D. K. Kim, A. J. Melville, B. M. Niedzielski, J. L. Yoder, *et al.*, Impact of ionizing radiation on superconducting qubit coherence, Nature **584**, 551 (2020).

[12] C. D. Wilen, S. Abdullah, N. A. Kurinsky, C. Stanford, L. Cardani, G. D'Imperio, C. Tomei, L. Faoro, L. B. Ioffe, C. H. Liu, *et al.*, Correlated charge noise and relaxation errors in superconducting qubits, Nature **594**, 369 (2021).

[13] C.-H. Liu, D. C. Harrison, S. Patel, C. D. Wilen, O. Rafferty, A. Shearrow, A. Ballard, V. Iaia, J. Ku, B. L. Plourde, *et al.*, Quasiparticle poisoning of superconducting qubits from resonant absorption of pair-breaking photons (2022), arXiv:2203.06577 [quant-ph].

[14] S. Diamond, V. Fatemi, M. Hays, H. Nho, P. D. Kurilovich, T. Connolly, V. R. Joshi, K. Serniak, L. Frunzio, L. I. Glazman, *et al.*, Distinguishing parity-switching mechanisms in a superconducting qubit (2022), arXiv:2204.07458 [quant-ph].

[15] E. T. Mannila, P. Samuelsson, S. Simbierowicz, J. T. Peltonen, V. Vesterinen, L. Grönberg, J. Hassel, V. F. Maisi, and J. P. Pekola, A superconductor free of quasiparticles for seconds, Nature Phys. **18**, 145 (2022).

[16] I. Alkhatib *et al.* (SuperCDMS Collaboration), Light dark matter search with a high-resolution athermal phonon detector operated above ground, Phys. Rev. Lett. **127**, 061801 (2021).

[17] A. H. Abdelhameed *et al.* (CRESST Collaboration), First results from the cresst-iii low-mass dark matter program, Phys. Rev. D **100**, 102002 (2019).

[18] P. Adari *et al.*, EXCESS workshop: Descriptions of rising low-energy spectra (2022), arXiv:2202.05097 [astro-ph.IM].

[19] L. Hehn *et al.* (EDELWEISS Collaboration), Improved EDELWEISS-III sensitivity for low-

TABLE VI. Summary of the passage fraction of triggered events in each of the 7 data taking periods, showing passage fraction for the baseline, slope, and χ^2 cuts.

Dataset No., Stress State	Baseline	Slope (Sequential)	Slope (Total)	χ^2 (Sequential)	χ^2 (Total)	Total Passage
1, Low Stress	0.959	0.976	0.965	0.973	0.973	0.921
2, Low Stress	0.964	0.977	0.971	0.981	0.981	0.935
3, Low Stress	0.964	0.974	0.969	0.990	0.990	0.942
4, Low Stress	0.967	0.976	0.972	0.980	0.980	0.935
5, Low Stress	0.963	0.974	0.969	0.975	0.975	0.927
6, Low Stress	0.969	0.977	0.974	0.981	0.981	0.939
7, Low Stress	0.969	0.977	0.973	0.979	0.979	0.936
1, High Stress	0.931	0.960	0.940	0.961	0.961	0.868
2, High Stress	0.935	0.961	0.944	0.966	0.966	0.877
3, High Stress	0.951	0.964	0.946	0.964	0.964	0.881
4, High Stress	0.939	0.964	0.946	0.925	0.925	0.846
5, High Stress	0.939	0.964	0.948	0.963	0.963	0.881
6, High Stress	0.940	0.963	0.950	0.968	0.968	0.887
7, High Stress	0.946	0.966	0.954	0.978	0.978	0.894
1, High + Low Stress						0.803
2, High + Low Stress						0.826
3, High + Low Stress						0.834
4, High + Low Stress						0.796
5, High + Low Stress						0.821
6, High + Low Stress						0.838
7, High + Low Stress						0.843

Cuts are applied sequentially. Sequential passage is the fraction of events that passed the previous cut which also pass this cut, total passage is the fraction of all events that pass this cut.

High + Low Stress total passage fractions show the passage fraction for the combined total high and low stress cuts.

mass WIMPs using a profile likelihood approach, Eur. Phys. J. C **76**, 548 (2016).

[20] T. Salagnac, J. Billard, J. Colas, D. Chaize, M. De Jesus, L. Dumoulin, J.-B. Filippini, J. Gascon, A. Juillard, H. Lattaud, *et al.* (RICOCHET Collaboration), Optimization and performance of the CryoCube detector for the future RICOCHET low-energy neutrino experiment (2021), arXiv:2111.12438 [physics.ins-det].

[21] M. Pyle, Low Energy Event Excess in Calorimeters (2022), EXCESS2022 Workshop.

[22] C. Strandhagen, Low Energy Excess in CRESST (2021), EXCESS2021 Workshop.

[23] A. Bespalov, M. Houzet, J. S. Meyer, and Y. V. Nazarov, Theoretical model to explain excess of quasiparticles in superconductors, Phys. Rev. Lett. **117**, 117002 (2016).

[24] K. W. Jones and H. W. Kraner, Energy lost to ionization by 254-eV ^{73}Ge atoms stopping in Ge, Phys. Rev. A **11**, 1347 (1975).

[25] J. Åström, P. C. F. Di Stefano, F. Pröbst, L. Stodolsky, J. Timonen, C. Bucci, S. Cooper, C. Cozzini, F. v. Feilitzsch, H. Kraus, *et al.*, Fracture processes observed with a cryogenic detector, Phys. Lett. A **356**, 262 (2006).

[26] I. Perepechko, *Low-Temperature Properties of Polymers* (Permagon Press, Inc., Elmsford, NY, 1980).

[27] K. D. Irwin and G. C. Hilton, Transition-edge sensors, in *Cryogenic Particle Detection*, edited by C. Enss (Springer Berlin Heidelberg, Berlin, Heidelberg, 2005) pp. 63–150.

[28] K. D. Irwin, S. W. Nam, B. Cabrera, B. Chugg, and B. A. Young, A quasiparticle-trap-assisted transition-edge sensor for phonon-mediated particle detection, Rev. Sci. Instrum. **66**, 5322 (1995).

[29] C. W. Fink *et al.* (CPD Collaboration), Performance of a large area photon detector for rare event search applications, Appl. Phys. Lett. **118**, 022601 (2021).

[30] C. W. Fink, S. L. Watkins, T. Aramaki, P. L. Brink, S. Ganjam, B. A. Hines, M. E. Huber, N. A. Kurinsky, R. Mahapatra, N. Mirabolfathi, *et al.*, Characterizing tes power noise for future single optical-phonon and infrared-photon detectors, AIP Adv. **10**, 085221 (2020).

[31] P. Du, D. Egana-Ugrinovic, R. Essig, and M. Sholapurkar, Sources of low-energy events in low-threshold dark-matter and neutrino detectors, Phys. Rev. X **12**, 011009 (2022).

[32] G. E. Totten, M. Tiryakioğlu, and O. Kessler, *Encyclopedia of Aluminum and Its Alloys* (CRC Press, Boca Raton, FL, 2018).

[33] D. K. Ward, W. A. Curtin, and Y. Qi, Aluminum–silicon interfaces and nanocomposites: A molecular dynamics study, Compos. Sci. Technol. **66**, 1151 (2006).

[34] J. M. Martinis, Saving superconducting quantum processors from qubit decay and correlated errors generated by gamma and cosmic rays, npj Quantum Inf. **7**, 90 (2021).

[35] T. Guruswamy, D. J. Goldie, and S. Withington, Quasiparticle generation efficiency in superconducting thin films, Supercond. Sci. Technol. **27**, 055012 (2014).

[36] P. Zyla *et al.* (Particle Data Group), Review of Particle Physics, Prog. Theor. Exp. Phys. **2020**, 083C01 (2020).

[37] R.-P. Riwar, A. Hosseinkhani, L. D. Burkhart, Y. Y. Gao, R. J. Schoelkopf, L. I. Glazman, and G. Catelani, Normal-metal quasiparticle traps for superconducting qubits, Phys. Rev. B **94**, 104516 (2016).